Applied Physics Letters ARTICLE scitation.org/journal/apl

Spin-voltage-driven efficient terahertz spin currents from the magnetic Weyl semimetals Co_2MnGa and Co_2MnAl

Cite as: Appl. Phys. Lett. **120**, 082401 (2022); doi: 10.1063/5.0080308
Submitted: 30 November 2021 · Accepted: 31 January 2022 ·
Published Online: 22 February 2022

Genaro Bierhance,[1,2] Anastasios Markou,[3] Oliver Gueckstock,[1,2] Reza Rouzegar,[1,2] Yannic Behovits,[1,2] Alexander L. Chekhov,[1,2] Martin Wolf,[1] Tom S. Seifert,[1,2] Claudia Felser,[3] and Tobias Kampfrath[1,2,a)]

AFFILIATIONS

[1]Department of Physical Chemistry, Fritz Haber Institute of the Max Planck Society, 14195 Berlin, Germany
[2]Department of Physics, Freie Universität Berlin, 14195 Berlin, Germany
[3]Max Planck Institute for Chemical Physics of Solids, Nöthnitzer Str. 40, 01187 Dresden, Germany

Note: This paper is part of the APL Special Collection on Ultrafast and Terahertz Spintronics.
[a)]**Author to whom correspondence should be addressed:** tobias.kampfrath@fu-berlin.de

ABSTRACT

Magnetic Weyl semimetals are an emerging material class that combines magnetic order and a topologically non-trivial band structure. Here, we study ultrafast optically driven spin injection from thin films of the magnetic Weyl semimetals Co_2MnGa and Co_2MnAl into an adjacent Pt layer by means of terahertz emission spectroscopy. We find that (i) Co_2MnGa and Co_2MnAl are efficient terahertz spin-current generators reaching efficiencies of typical 3d-transition-metal ferromagnets such as Fe. (ii) The relaxation of the spin current provides an estimate of the electron-spin relaxation time of Co_2MnGa (170 fs) and Co_2MnAl (100 fs), which is comparable to Fe (90 fs). Both observations are consistent with a simple analytical model and highlight the large potential of magnetic Weyl semimetals as spin-current sources in terahertz spintronic devices. Finally, our results provide a strategy to identify magnetic materials that offer maximum spin-current amplitudes for a given deposited optical energy density.

Magnetic Weyl semimetals (WSM) are a new class of materials with properties that are interesting from both a scientific and applied viewpoint.[1–5] Model representatives are the ferromagnetic Heusler compounds Co_2MnGa (CMG) and Co_2MnAl (CMA). CMG exhibits symmetry-protected, topological nodal-line band crossings and drumhead surface states,[6] whereas CMA is considered a nodal-line WSM candidate.[7,8] Their high spin polarization at the Fermi energy,[3,9,10] the large anomalous Hall effect,[7,11] and anomalous Nernst effect[12,13] make them promising candidates for efficient spin injection into an adjacent material.

It is highly interesting to push the speed of spin injection to femtosecond (fs) time scales and, thus, terahertz (THz) bandwidth by excitation with fs laser pulses, as it was previously shown for other magnetically ordered materials.[14,15] On the one hand, the resulting THz spin transport can be used to generate spin torque,[16,17] to switch magnetic order,[18] and to generate THz electromagnetic pulses for spectroscopy and photonic applications.[19–27] On the other hand, THz spin transport provides insight into the electron-spin relaxation time,[28] which describes the time it takes until electron and spin degrees of freedom equilibrate with each other.[18] Recent studies on Co_2MnSi and Co_2FeAl have already shown the large potential of Co-based Heusler alloys in the context of spintronic THz emitters.[29,30]

In this work, we use THz emission spectroscopy to characterize the photoinduced ultrafast spin-injection efficiency of CMG and CMA thin films into an adjacent Pt layer and the shape of the resulting spin-current pulses. A comparison with the standard ferromagnet Fe reveals a high efficiency of magnetic WSMs CMG and CMA as ultrafast spin-current generators. The relaxation time of the spin current pulse is dominated by the electron-spin equilibration, for which an upper limit of 170 and 100 fs is inferred for CMG and CMA, respectively. These values are about 90% and 10% higher than for the Fe reference.

The principle of our THz emission experiments is illustrated in Fig. 1.[19,31,32] The samples are sub||F|Pt stacks consisting of a ferromagnetic layer F and a Pt layer on an optically transparent substrate sub.

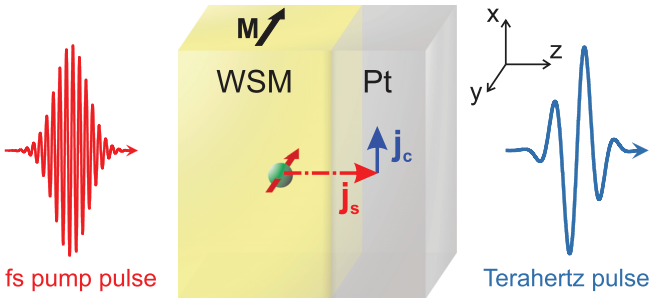

FIG. 1. Laser-induced spin injection from a magnetic WSM. The sample is a F|Pt stack where the ferromagnetic layer F consists of the WSM CMG or CMA or the reference magnet Fe. Excitation by a femtosecond (fs) pump pulse launches a spin current with density j_s from F with magnetization $\boldsymbol{M}$ into the Pt layer. Spin–orbit interaction converts j_s into a transverse charge current j_c that acts as a source of a THz electromagnetic pulse. The spin-to-charge-current conversion is assumed to be dominated by the inverse spin Hall effect in Pt.

The magnetization $\boldsymbol{M}$ of the F-layer is saturated by an external magnetic field of the order of 100 mT. Magnetic hysteresis loops are shown in Fig. S1. The F|Pt thin-film stack is excited by a fs pump pulse (duration ≈20 fs, center wavelength 800 nm, energy ≈2 nJ, repetition rate ≈80 MHz) from a Ti:sapphire laser oscillator. The excitation induces a transient spin voltage that launches a spin current with density j_s from the ferromagnetic layer F into the Pt layer. Due to spin–orbit interaction, the spin current in Pt is converted into a transverse charge current perpendicular to the sample magnetization by the inverse spin Hall effect (ISHE), giving rise to the emission of a THz electromagnetic pulse (see Fig. 1).

The emitted THz pulse is measured by electro-optic sampling in ZnTe(110) or GaP(110) crystals (thickness 1 mm and 250 μm, respectively).[33] The resulting signal $S(t)$ vs time t is related to the THz electric field $E(t)$ directly behind the sample by a linear transfer function that accounts for the propagation of the THz pulse to the electro-optic crystal and the detection process. To connect $S(t)$ to the spin current, we note that $E(t)$ is in the frequency domain given by[19]

$$E(\omega) \propto Z(\omega)\sigma_{\mathrm{SH}}(\omega)j_s(\omega). \tag{1}$$

Here, $\omega/2\pi$ is the frequency, $j_s(\omega)$ is the spin-current density right behind the F/N interface, $\sigma_{\mathrm{SH}}(\omega)$ is the spin Hall conductivity of N, and $Z(\omega)$ is the sample impedance. We note that Eq. (1) is equivalent to previously used versions (see Refs. 34 and 35 and the supplementary material). Other possible contributions to the THz emission signal will be discussed further below.

Note that the root mean square (rms) of $j_s(t)$ in the time domain scales with the deposited pump energy density [inset of Fig. 2(a)], that is, $\mathrm{rms}\, j_s \propto A/d$, where A is the pump absorptance of our sample, and d is the thickness of the metal stack. Thus, $\mathrm{rms}\, j_s d/A$ provides a figure of merit (FOM) that characterizes the spin-injection efficiency of the F material into Pt. Following Eq. (1), we, therefore, compare[32]

$$\mathrm{FOM} = \frac{d}{A\overline{|Z|}}\,\mathrm{rms}\, S \tag{2}$$

for F|Pt samples with F=CMG and CMA to a reference sample with F=Fe. In Eq. (2), the sample impedance $Z(\omega)$ was approximated by

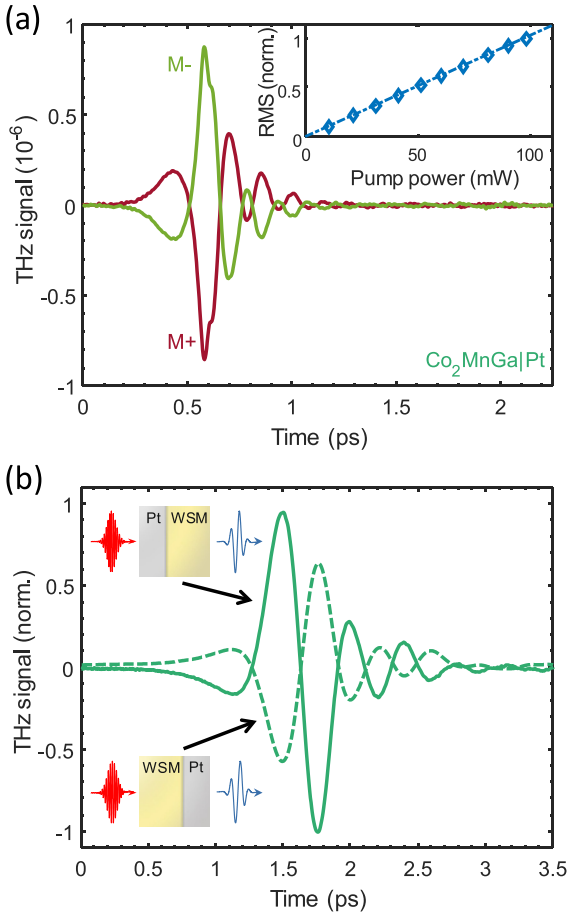

FIG. 2. THz emission from a WSM|Pt stack. (a) THz-emission signal $S(t, \pm\boldsymbol{M})$ from CMG|Pt for magnetizations $\pm\boldsymbol{M}$ as obtained with a 250 μm thick GaP(110) electro-optic detector. Inset: Normalized THz-emission-signal amplitude (root mean square, rms) of the signal component odd in $\boldsymbol{M}$ vs pump power. The dashed line is a linear fit through the origin. (b) THz emission signals $S(t)$ odd in $\boldsymbol{M}$ [see Eq. (3)] from MgO||CMG|Pt and the same sample physically turned by 180° (Pt|CMG||MgO). The signals are obtained with a 1 mm thick ZnTe electro-optic detector and corrected for propagation effects (dispersion, absorption) through the MgO substrate.[28] Thus, the curves refer to CMG|Pt and Pt|CMG films with an MgO substrate on either side, which is omitted in the sample schematics.

$\overline{|Z|}$, i.e., $|Z(\omega)|$ averaged over 1–5 THz. Note that we replaced the rms of the THz electric field E behind the sample by the rms of the THz signal S, since E and S are related by an identical transfer function for all samples measured in our experiment. Consequently, the FOM of Eq. (2) should only be used as a relative measure, i.e., for comparison of different samples measured in the same THz emission setup.

We study two-layer stacks Fe(3 nm)|Pt(3 nm), CMG(20 nm)|Pt(2 nm), and CMA(20 nm)|Pt(3 nm) grown on MgO substrates (0.5 mm).[11] The CMG|Pt and CMA|Pt films are additionally capped with a Si(3 nm) layer. The thin films are deposited by magnetron sputtering. Characterization by x-ray diffraction and atomic force microscopy (see Figs. S2 and S3) shows that all of the studied magnetic WSM samples have similar surface morphologies and a surface roughness of less than 1 nm (with and without Pt and Si capping).

The sample impedance $Z(\omega)$ is determined by THz transmission spectroscopy,[36] and its modulus is found to change by less than 2% over the interval 1–5 THz (see Figs. S4 and S5). This observation justifies the approximation $|Z(\omega)| = \overline{|Z|}$ introduced above. The sample absorptance A is inferred by optical transmission and reflection measurements using the pump beam.[36] Table I compiles the values of A and $\overline{|Z|}$ and other quantities of our samples.

Typical THz signals $S(t, \pm\boldsymbol{M})$ for opposite sample magnetizations $\pm\boldsymbol{M}$ are displayed in Fig. 2(a). The signal reverses almost completely with $\boldsymbol{M}$, showing that the THz signal is predominantly of magnetic origin. As we are only interested in effects odd in the sample magnetization, we focus on the signal

$$S(t) = \frac{S(t, +\boldsymbol{M}) - S(t, -\boldsymbol{M})}{2} \tag{3}$$

in the following. The signal components even in $\boldsymbol{M}$ are about one order of magnitude smaller (see Fig. S6). The amplitude of $S(t)$ exhibits a minor dependence on the sample azimuth of about 5% of the total signal, consistent with the notion that the primary function of the pump pulse is just to deposit energy in the metal film.

Figure 2(b) shows the THz emission signal $S(t)$ from MgO||CMG|Pt. When the sample is turned by 180°, resulting in Pt|CMG||MgO, the sign of j_s and, thus, the THz signal reverses[36] but exhibits a larger amplitude. Note that the altered propagation of the pump pulse to the metal film and the THz pulse away from the metal film due to sample turning were corrected for by a suitable reference measurement.[28] Therefore, we ascribe the different emission amplitudes from the measurements of MgO||CMG|Pt and Pt|CMG||MgO to the different amplitude of the pump field at the CMG/Pt interface. For MgO||CMG|Pt, the pump field at the CMG/Pt interface is significantly smaller than for Pt|CMG||MgO because the pump field is attenuated by 20 nm of CMG before reaching the interface.

Calculations of the pump propagation inside the metal stack show that the substrate-corrected amplitude ratio of the pump intensity at the CMG/Pt interface in the Pt|CMG sample and in the reversed CMG|Pt sample amounts to 1.34 (see Fig. S7), which is in reasonable agreement with the amplitude ratio of 1.59 of the two THz signals in Fig. 2(b). We conclude that the emission from CMG|Pt has electric-dipole symmetry and is determined by the pump-field amplitude at the CMG/Pt interface.[28]

Figure 3(a) shows scaled THz signals $S(t)d/A\overline{|Z|}$ from the three F|Pt samples, where F denotes the Fe reference and the magnetic WSMs CMG and CMA. The scaling factor $d/A\overline{|Z|}$ allows for a direct comparison in terms of spin-injection efficiency [see Eq. (2)]. We find that the three signals exhibit very similar dynamics. Therefore, their relative rms amplitudes are a direct measure of the spin-injection efficiency. Note that both CMG|Pt and CMA|Pt reach, respectively, 71% and 76% of the rms amplitude of Fe, which is in good agreement with the ratio of the peak values seen in Fig. 3(a). Thus, the two WSMs have a FOM of spin-injection efficiency that can compete with that of Fe.

Figure 3(b) shows the amplitude spectra of the three THz emission signals. As expected from the time-domain signals [Fig. 3(a)], the spectra have very similar shape and comparable amplitude. We note that the dip at 8 THz and the feature at 12 THz are signatures of the electro-optic detection process in GaP.[31,33,37]

To extract the dynamics $j_s(t)$ of the spin-current density (Fig. 1), we measure the transfer function of our setup, use it to calculate back from the measured THz signal $S(t)$ to the THz field $E(t)$ and eventually employ Eq. (1).[38,39] The resulting traces $j_s(t)$ are shown in Fig. 3(c). As expected from the THz signals [Fig. 3(a)], the spin currents show approximately identical dynamics for all three samples: an instantaneous rise that is limited by our effective time resolution of about 40 fs (see Ref. 28), followed by a decay on a 100 fs timescale.

The extracted $j_s(t)$ can be well fit by an exponentially decaying Heaviside step function $\Theta(t)e^{-t/\tau}$, convoluted with a Gaussian with 40 fs full width at half maximum, which accounts for our effective time resolution. We obtain time constants of $\tau = 170$, 100, and 90 fs for CMG|Pt, CMA|Pt and Fe|Pt, respectively. Previous work[28] has shown that the inverse time constant $\tau^{-1} = \tau_{ep}^{-1} + \tau_{es}^{-1}$ is a sum of the inverse time constants of electron-phonon (τ_{ep}^{-1}) and electron-spin (τ_{es}^{-1}) equilibration. In simple ferromagnetic metals, such as $Co_{70}Fe_{30}$ or $Ni_{80}Fe_{20}$, τ_{ep} is typically substantially longer than τ_{es}.[28] Therefore, we expect that the time constant τ measured for CMG and CMA is a good estimate of τ_{es}.

Note that τ_{es}^{-1}, in turn, is a sum of terms due to electron spin flips and spin transport out of F. However, for F|Pt stacks with simple ferromagnetic metals F, transport was found to make a minor contribution.[28] Thus, τ is a lower bound to the time τ_{es} it takes electron and spin degrees of freedom to equilibrate with each other due to spin flips in F.

To discuss our results, we first note that our approach strongly relies on Pt as a reliable spin-current detector, whose performance should not differ significantly between the three samples studied here. Indeed, the intrinsic component of the spin Hall conductivity was shown to have less than 10% dispersion between Pt layers with different quality and growth conditions.[40] The extrinsic component due to skew scattering is estimated to contribute less than 10% to the total spin-to-charge-current conversion (S2C) of Pt.[36] In addition, the low

TABLE I. Sample parameters. The columns show the sample, pump absorptance A, total metal-stack thickness d, and DC conductivity G_{DC}^{4pp}/d averaged over d, where the DC sheet conductance G_{DC}^{4pp} is determined with a four-point probe system. The absolute value $\overline{|Z|}$ of the sample sheet impedance (averaged over 1–5 THz), the DC conductivity $G(0)/d$ (averaged over d), and the Drude model damping rate Γ_{eff} are obtained by THz transmission spectroscopy. For the sample structure, the numbers in brackets denote the layer thickness in nanometer.

Sample	A	d (nm)	$\overline{\lvert Z\rvert}$ (Ω)	G_{DC}^{4pp}/d (MS/m)	$G(0)/d$ (MS/m)	$\Gamma_{eff}/2\pi$ (THz)
MgO||Co_2MnGa(20)|Pt(2)|Si(3)	0.61	25	39	0.71	0.60	19
MgO||Co_2MnAl(20)|Pt(3)|Si(3)	0.63	26	50	-	0.35	25
MgO||Fe(3)|Pt(3)	0.54	6	43	2.13	2.07	19

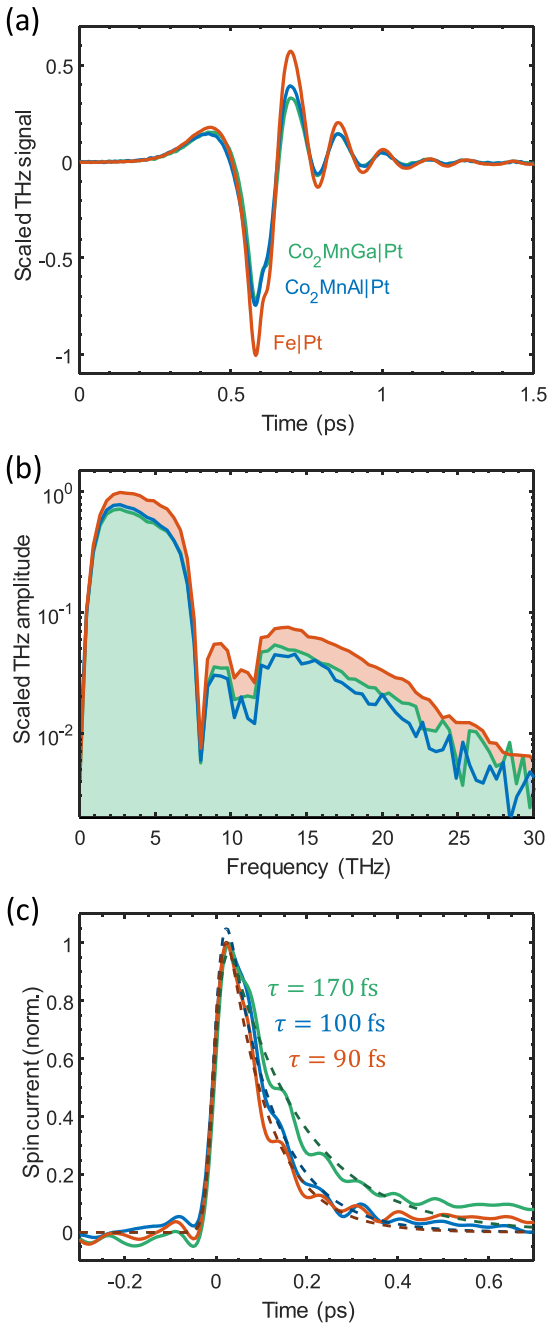

FIG. 3. Comparison of THz spin transport in WSM|Pt vs Fe|Pt. (a) Scaled THz emission signals $S(t)d/A|\overline{Z}|$ odd in $\boldsymbol{M}$ from CMG|Pt, CMA|Pt, and Fe|Pt as obtained with a 250 μm thick GaP electro-optic detector. Here, A, $|\overline{Z}|$, and d are the pump absorptance, THz impedance, and thickness of the sample. The scaled signal is a figure of merit in terms of spin-injection efficiency [see Eq. (2)]. (b) Corresponding frequency spectra for the waveforms in (a). (c) Normalized spin-current-density dynamics extracted from the THz-emission signals in (a). The dashed lines are single-sided mono-exponential fits convoluted with a Gaussian (40 fs full width at half maximum) along with the obtained relaxation times τ. In panels (a) and (b), signals are normalized to the peak signal from the Fe|Pt reference.

surface roughness of all samples (see above and Fig. S3) indicates smooth CMG/Pt and CMA/Pt interfaces and, therefore, an even smaller contribution by skew scattering.

We also note that Eq. (1) neglects a number of odd-in-$\boldsymbol{M}$ contributions to the THz field emission other than S2C in Pt. (1) Magnetic-dipole emission due to ultrafast demagnetization typically has a two orders of magnitude smaller amplitude than the total signal from F|N samples.[28] In terms of transport, various bulk and interface contributions of spin currents and the subsequent S2C lead to THz emission. (2) Spin currents in the F bulk arise from pump-induced gradients of excess energy. (3) Likewise, the two F interfaces can differ in terms of spin transport or S2C. Consequently, a nonzero spatial integral of the transverse charge current can result.[41] We estimate the strength of (1)–(3) by measuring THz emission from a single CMG layer and find that they can contribute 5%–10% to the total signal from the CMG|Pt sample (Fig. S8).

Finally, (4) spin currents across the F/N interface arise from a pump-induced interfacial gradient of the spin voltage.[28] S2C may proceed not only by the ISHE in the Pt bulk, but also by the ISHE in the F bulk and by the inverse Rashba–Edelstein effect (IREE) at the F/N interface.[42–44] To estimate the ISHE in the F bulk, we refer to Ref. 36, where the ISHE of N in Fe|N stacks was disabled by using N=Cu instead of Pt. Based on the anomalous Hall conductivities of Fe,[42] CMG,[11] and CMA,[7] we obtain an upper limit of 10%–20% for the contribution of the ISHE of CMG and CMA in our CMG|Pt and CMA|Pt samples (see supplementary material). Finally, the IREE of the prototypical IREE interface Ag/Bi was found to contribute less than 10% compared to the ISHE of Pt.[43] We conclude that S2C by the ISHE in the Pt bulk is the dominant THz emission mechanism in our CMG|Pt and CMA|Pt samples.

Our measurements, thus, show that (i) the efficiency of laser-induced spin injection of the magnetic WSMs CMG and CMA is almost as high (71% and 76%, respectively) as that of Fe [Fig. 3(a)], and (ii) the electron-spin relaxation time τ_{es} of CMG and CMA is only 90% and 10% longer than for Fe [Fig. 3(c)]. Both results appear surprising at first glance because CMG and CMA are rather different materials than Fe as they possess semimetal-like cone-shaped electronic bands near the Fermi energy. However, in addition to these topologically protected bands, there are "trivial" bands that contribute a significant electronic density of states at the Fermi energy.

To discuss the results (i) and (ii) in a more quantitative manner, we make use of the simple analytic spin-flip and transport model of Ref. 28. In the framework of this model, observation (ii) points to similar values of the product $P_{sf}D^{\uparrow}D^{\downarrow}/\chi_m$, which quantifies the contribution of electronic spin flips to the ultrafast decay of the spin voltage of the ferromagnetic layer.[28] Here, P_{sf} scales with the spin-flip matrix element, $D^{\uparrow}$ and $D^{\downarrow}$ denote the density of states of spin-up and spin-down electrons at the Fermi level of F, and χ_m is the spin part of the magnetic susceptibility. The values of $D^{\uparrow}$ and $D^{\downarrow}$ for Fe [$D^{\uparrow} \approx 1.7 \times 10^{28}$ and $D^{\downarrow} \approx 6.8 \times 10^{28}/(\text{eV m}^3)$][45] are significantly larger than for CMG [$D^{\uparrow} \approx 0.4 \times 10^{28}$ and $D^{\downarrow} \approx 3.1 \times 10^{28}/(\text{eV m}^3)$][46,47] and CMA [$D^{\uparrow} \approx 0.6 \times 10^{28}$ and $D^{\downarrow} \approx 3.2 \times 10^{28}/(\text{eV m}^3)$].[48,49] Because the measured τ_{es} of Fe, CMG, and CMA are similar [Fig. 3(c)], we conclude that the ratio P_{sf}/χ_m of spin-flip matrix element and magnetic susceptibility of CMG and CMA is one order of magnitude larger than that of Fe. This result may point to a significantly stronger effective spin–orbit coupling and/or smaller χ_m in CMG and CMA than in Fe. Indeed, in the framework of the Stoner model,[50] one expects a

significantly smaller magnetic susceptibility for CMG and CMA than for Fe because of the significantly smaller density of states $D^{\uparrow}$ and $D^{\downarrow}$ of CMG and CMA and the roughly comparable Curie temperatures[11,51,52] of all three materials.

Regarding result (i), the peak spin-current amplitude directly after excitation by the pump pulse can be shown to roughly scale with[28] $M'_{eq}(T_0)T_{tr}^{\uparrow}D^{\uparrow}/D^{\downarrow}\chi_m$, where $D^{\uparrow} \ll D^{\downarrow}$ was used. In this expression, $M'_{eq}(T_0)$ is the temperature derivative of the F equilibrium magnetization M_{eq} at the sample temperature T_0 before excitation, and $T_{tr}^{\uparrow}$ is the transmission coefficient of spin-up electrons through the F/Pt interface. We expect similar values for $M'_{eq}(T_0)$ for CMG, CMA, and Fe: While the saturation magnetization of Fe is about twice larger than that of CMG, this ratio is compensated by the lower Curie temperature of CMG[11,51] (700 vs 1000 K) resulting in a larger gradient $M'_{eq}(T_0)$ at $T_0 = 300$ K. Likewise, the ratio $D^{\uparrow}/D^{\downarrow}$ is comparable for all three materials (see above). Thus, because the measured peak spin-current densities of Fe, CMG, and CMA are similar [Fig. 3(a)], the ratio $T_{tr}^{\uparrow}/\chi_m$ is of the same order of magnitude for all three materials. As χ_m is likely smaller for CMG and CMA (see above), the same is true for the transmission coefficient $T_{tr}^{\uparrow}$. Therefore, our observations (i) and (ii) along with the simple analytical model of Ref. 28 yield interesting information on key parameters of CMG and CMA.

In conclusion, we measure ultrafast spin current generation by fs laser pulses in CMG|Pt and CMA|Pt stacks. We find that (i) for a given excitation density, the spin current amplitudes are comparable to Fe|Pt stacks, thereby identifying CMG and CMA as efficient ultrafast light-driven spin-current injectors or, in other words, efficient sources of transient spin voltages. (ii) The relaxation time of the spin current is somewhat longer than for Fe and provides an estimate of the electron-spin relaxation time of CMG and CMA due to spin flips. Both results are consistent with a simple analytical model.[28] Therefore, our consideration of the spin current amplitude can be used as a general strategy to identify F-material candidates that deliver maximum spin current amplitudes for a given deposited optical energy density for highly efficient THz spintronic devices.

See the supplementary material for further details.

The authors thank Martin Jourdan and Gerhard Jakob (Johannes-Gutenberg-Universität Mainz, Germany) for providing the Fe|Pt sample. They acknowledge funding by the European Union H2020 program through the FET projects SKYTOP/Grant No. 824123 and the German Research Foundation through the Collaborative Research Center SFB TRR 227 "Ultrafast spin dynamics" (projects A05 and B02).

AUTHOR DECLARATIONS

Conflict of Interest

The authors have no conflicts to disclose.

DATA AVAILABILITY

The data associated with this work are openly available at Zenodo, https://doi.org/10.5281/zenodo.5748041, Ref. 53.

REFERENCES

[1]W. Ning and Z. Mao, APL Mater. **8**, 090701 (2020).
[2]B. Cheng, Y. Wang, D. Barbalas, T. Higo, S. Nakatsuji, and N. Armitage, Appl. Phys. Lett. **115**, 012405 (2019).
[3]P. Swekis, A. S. Sukhanov, Y.-C. Chen, A. Gloskovskii, G. H. Fecher, I. Panagiotopoulos, J. Sichelschmidt, V. Ukleev, A. Devishvili, A. Vorobiev, D. S. Inosov, S. T. B. Goennenwein, C. Felser, and A. Markou, Nanomaterials **11**, 251 (2021).
[4]C. Guo, B. Zhao, D. Huang, and S. Fan, ACS Photonics **7**, 3257 (2020).
[5]G. Tang, J. Chen, and L. Zhang, ACS Photonics **8**, 443 (2021).
[6]I. Belopolski, K. Manna, D. S. Sanchez, G. Chang, B. Ernst, J. Yin, S. S. Zhang, T. Cochran, N. Shumiya, H. Zheng, B. Singh, G. Bian, D. Multer, M. Litskevich, X. Zhou, S.-M. Huang, B. Wang, T.-R. Chang, S.-Y. Xu, A. Bansil, C. Felser, H. Lin, and M. Z. Hasan, Science **365**, 1278 (2019).
[7]P. Li, J. Koo, W. Ning, J. Li, L. Miao, L. Min, Y. Zhu, Y. Wang, N. Alem, C.-X. Liu, Z. Mao, and B. Yan, Nat. Commun. **11**, 3476 (2020).
[8]J. Kübler and C. Felser, Europhys. Lett. **114**, 47005 (2016).
[9]C. Guillemard, S. Petit-Watelot, L. Pasquier, D. Pierre, J. Ghanbaja, J. C. Rojas-Sánchez, A. Bataille, J. Rault, P. Le Fèvre, F. Bertran, and S. Andrieu, Phys. Rev. Appl. **11**, 064009 (2019).
[10]J.-C. Tung and G.-Y. Guo, New J. Phys. **15**, 033014 (2013).
[11]A. Markou, D. Kriegner, J. Gayles, L. Zhang, Y.-C. Chen, B. Ernst, Y.-H. Lai, W. Schnelle, Y.-H. Chu, Y. Sun, and C. Felser, Phys. Rev. B **100**, 054422 (2019).
[12]H. Reichlova, R. Schlitz, S. Beckert, P. Swekis, A. Markou, Y.-C. Chen, D. Kriegner, S. Fabretti, G. H. Park, A. Niemann, S. Sudheendra, A. Thomas, K. Nielsch, C. Felser, and S. T. B. Goennenwein, Appl. Phys. Lett. **113**, 212405 (2018).
[13]G.-H. Park, H. Reichlova, R. Schlitz, M. Lammel, A. Markou, P. Swekis, P. Ritzinger, D. Kriegner, J. Noky, J. Gayles, Y. Sun, C. Felser, K. Nielsch, S. T. B. Goennenwein, and A. Thomas, Phys. Rev. B **101**, 060406 (2020).
[14]T. J. Huisman, C. Ciccarelli, A. Tsukamoto, R. V. Mikhaylovskiy, T. Rasing, and A. V. Kimel, Appl. Phys. Lett. **110**, 072402 (2017).
[15]M. Hofherr, P. Maldonado, O. Schmitt, M. Berritta, U. Bierbrauer, S. Sadashivaiah, A. Schellekens, B. Koopmans, D. Steil, and M. Cinchetti, Phys. Rev. B **96**, 100403 (2017).
[16]I. Razdolski, A. Alekhin, N. Ilin, J. P. Meyburg, V. Roddatis, D. Diesing, U. Bovensiepen, and A. Melnikov, Nat. Commun. **8**, 15007 (2017).
[17]M. L. M. Lalieu, R. Lavrijsen, R. A. Duine, and B. Koopmans, Phys. Rev. B **99**, 184439 (2019).
[18]A. Kirilyuk, A. V. Kimel, and T. Rasing, Rep. Prog. Phys. **76**, 026501 (2013).
[19]T. Seifert, S. Jaiswal, U. Martens, J. Hannegan, L. Braun, P. Maldonado, F. Freimuth, A. Kronenberg, J. Henrizi, I. Radu, E. Beaurepaire, Y. Mokrousov, P. M. Oppeneer, M. Jourdan, G. Jakob, D. Turchinovich, L. M. Hayden, M. Wolf, M. Münzenberg, M. Kläui, and T. Kampfrath, Nat. Photonics **10**, 483 (2016).
[20]D. Yang, J. Liang, C. Zhou, L. Sun, R. Zheng, S. Luo, Y. Wu, and J. Qi, Adv. Opt. Mater. **4**, 1944 (2016).
[21]Y. Wu, M. Elyasi, X. Qiu, M. Chen, Y. Liu, L. Ke, and H. Yang, Adv. Mater. **29**, 1603031 (2017).
[22]G. Torosyan, S. Keller, L. Scheuer, R. Beigang, and E. T. Papaioannou, Sci. Rep. **8**, 1311 (2018).
[23]R. Schneider, M. Fix, R. Heming, S. Michaelis de Vasconcellos, M. Albrecht, and R. Bratschitsch, ACS Photonics **5**, 3936 (2018).
[24]E. T. Papaioannou and R. Beigang, Nanophotonics **10**, 1243 (2021).
[25]Z. Feng, H. Qiu, D. Wang, C. Zhang, S. Sun, B. Jin, and W. Tan, J. Appl. Phys. **129**, 010901 (2021).
[26]L. Cheng, Z. Li, D. Zhao, and E. E. Chia, APL Mater. **9**, 070902 (2021).
[27]W. Wu, C. Yaw Ameyaw, M. F. Doty, and M. B. Jungfleisch, J. Appl. Phys. **130**, 091101 (2021).
[28]R. Rouzegar, L. Brandt, L. Nadvornik, D. A. Reiss, A. L. Chekhov, O. Gueckstock, C. In, M. Wolf, T. S. Seifert, P. W. Brouwer, G. Woltersdorf, and T. Kampfrath, "Laser-induced terahertz spin transport in magnetic nanostructures arises from the same force as ultrafast demagnetization," arXiv:2103.11710 (2021).
[29]R. Gupta, S. Husain, A. Kumar, R. Brucas, A. Rydberg, and P. Svedlindh, Adv. Opt. Mater. **9**, 2001987 (2021).
[30]Y. Sasaki, Y. Takahashi, and S. Kasai, Appl. Phys. Express **13**, 093003 (2020).
[31]T. Kampfrath, M. Battiato, P. Maldonado, G. Eilers, J. Nötzold, S. Mährlein, V. Zbarsky, F. Freimuth, Y. Mokrousov, S. Blügel, M. Wolf, I. Radu, P. M. Oppeneer, and M. Münzenberg, Nat. Nanotechnol. **8**, 256 (2013).

[32]T. Seifert, U. Martens, S. Günther, M. A. W. Schoen, F. Radu, X. Z. Chen, I. Lucas, R. Ramos, M. H. Aguirre, P. A. Algarabel, A. Anadón, H. S. Körner, J. Walowski, C. Back, M. R. Ibarra, L. Morellón, E. Saitoh, M. Wolf, C. Song, K. Uchida, M. Münzenberg, I. Radu, and T. Kampfrath, Spin **7**, 1740010 (2017).
[33]A. Leitenstorfer, S. Hunsche, J. Shah, M. C. Nuss, and W. H. Knox, Appl. Phys. Lett. **74**, 1516 (1999).
[34]T. S. Seifert, N. M. Tran, O. Gueckstock, S. M. Rouzegar, L. Nadvornik, S. Jaiswal, G. Jakob, V. V. Temnov, M. Münzenberg, M. Wolf, M. Kläui, and T. Kampfrath, J. Phys. D: Appl. Phys. **51**, 364003 (2018).
[35]T. H. Dang, J. Hawecker, E. Rongione, G. B. Flores, D. Q. To, J. C. Rojas-Sanchez, H. Nong, J. Mangeney, J. Tignon, F. Godel, S. Collin, P. Seneor, M. Bibes, A. Fert, M. Anane, J.-M. George, L. Vila, M. Cosset-Cheneau, D. Dolfi, R. Lebrun, P. Bortolotti, K. Belashchenko, S. Dhillon, and H. Jaffrès, Appl. Phys. Rev. **7**, 041409 (2020).
[36]O. Gueckstock, L. Nádvorník, M. Gradhand, T. S. Seifert, G. Bierhance, R. Rouzegar, M. Wolf, M. Vafaee, J. Cramer, M. A. Syskaki, G. Woltersdorf, I. Mertig, G. Jakob, M. Kläui, and T. Kampfrath, Adv. Mater. **33**, 2006281 (2021).
[37]T. Kampfrath, J. Nötzold, and M. Wolf, Appl. Phys. Lett. **90**, 231113 (2007).
[38]L. Braun, G. Mussler, A. Hruban, M. Konczykowski, T. Schumann, M. Wolf, M. Münzenberg, L. Perfetti, and T. Kampfrath, Nat. Commun. **7**, 13259 (2016).
[39]T. S. Seifert, S. Jaiswal, J. Barker, S. T. Weber, I. Razdolski, J. Cramer, O. Gueckstock, S. F. Maehrlein, L. Nadvornik, S. Watanabe, C. Ciccarelli, A. Melnikov, G. Jakob, M. Münzenberg, S. T. B. Goennenwein, G. Woltersdorf, B. Rethfeld, P. W. Brouwer, M. Wolf, M. Kläui, and T. Kampfrath, Nat. Commun. **9**, 2899 (2018).
[40]E. Sagasta, Y. Omori, M. Isasa, M. Gradhand, L. E. Hueso, Y. Niimi, Y. Otani, and F. Casanova, Phys. Rev. B **94**, 060412 (2016).
[41]Q. Zhang, Z. Luo, H. Li, Y. Yang, X. Zhang, and Y. Wu, Phys. Rev. Appl. **12**, 054027 (2019).
[42]V. P. Amin, J. Li, M. D. Stiles, and P. M. Haney, Phys. Rev. B **99**, 220405 (2019).
[43]M. B. Jungfleisch, Q. Zhang, W. Zhang, J. E. Pearson, R. D. Schaller, H. Wen, and A. Hoffmann, Phys. Rev. Lett. **120**, 207207 (2018).
[44]C. Zhou, Y. P. Liu, Z. Wang, S. J. Ma, M. W. Jia, R. Q. Wu, L. Zhou, W. Zhang, M. K. Liu, Y. Z. Wu, and J. Qi, Phys. Rev. Lett. **121**, 086801 (2018).
[45]V. L. Moruzzi, J. F. Janak, and A. R. Williams, in *Calculated Electronic Properties of Metals* (Elsevier, 2013).
[46]B. Hamad, J. Appl. Phys. **115**, 113905 (2014).
[47]Co_2MnGa ($MnCo_2Ga$ rt) Crystal Structure Datasheet From *Pauling File Multinaries*, Springer Materials, edited by P. Villars and K. Cenzual [Springer-Verlag Berlin Heidelberg; Material Phases Data System (MPDS)/Switzerland; and National Institute for Materials Science (NIMS), Japan, 2012].
[48]B. Aktas and F. Mikailov, in *Advances in Nanoscale Magnetism: Proceedings of the International Conference on Nanoscale Magnetism (ICNM-2007), Istanbul, Turkey, 25–29 June* (Springer Science & Business Media, 2008).
[49]Co_2MnAl ($MnCo_2Al$ rt) Crystal Structure Datasheet from *Pauling File Multinaries*, Springer Materials, edited by P. Villars and K. Cenzual [Springer-Verlag Berlin Heidelberg; Material Phases Data System (MPDS)/Switzerland; and National Institute for Materials Science (NIMS), Japan, 2012].
[50]W. Nolting and A. Ramakanth, in *Quantum Theory of Magnetism* (Springer Science & Business Media, 2009).
[51]J. M. D. Coey, in *Magnetism and Magnetic Materials* (Cambridge University Press, 2010).
[52]T. Ryba, Z. Vargova, J. Kovac, P. Diko, V. Kavečanský, S. Piovarči, C. Garcia, and R. Varga, IEEE Trans. Magn. **51**, 2600103 (2015).
[53]G. Bierhance, A. Markou, O. Gueckstock, R. Rouzegar, Y. Behovits, A. Chekhov, M. Wolf, T. S. Seifert, C. Felser, and T. Kampfrath, (2021). "Spin-voltage-driven efficient terahertz spin currents from the magnetic Weyl semimetals Co_2MnGa and Co_2MnAl," Zenodo. https://doi.org/10.5281/zenodo.5748041.